Ring-Core Photonic Quasi-Crystal Fiber With 34 Polarization Multiplexing Modes

Wei Wei, Yitong Wang, Hongyang Zhao, Ziming Dong, Liqin Tang, Lei Ding, and Yigang Li

***Abstract*—We propose a ring-core photonic quasi-crystal fiber (RC-PQCF) featuring a ring-shaped fiber core and two symmetrical SiO_2 stress-applying parts (SAPs). By optimizing the mole percentage of GeO_2 and geometrical parameters of the fiber, the design supports 34 full vector polarization modes (FV-PMs). The effective refractive index difference (Δn_{eff}) of adjacent FV-PMs is larger than 1.07×10^{-4} at 1550 nm. The confinement loss (α) of FV-PMs is less than 10^{-6}, which is sufficient to confine the light field in the ring-core. Through numerical analysis, broadband performance is investigated subsequently in the 1500–1600 nm. The dispersion (D_λ) of FV-PMs is less than $138.14\ \mathrm{ps \cdot nm^{-1} \cdot km^{-1}}$ and maintains a flat trend. The mode field area (A_{eff}) of FV-PMs is larger compared to single mode fibers and the nonlinear coefficient (γ) of FV-PMs is within $(6.97 \times 10^{-4}, 1.54 \times 10^{-3})\ \mathrm{m^{-1} \cdot W^{-1}}$ in the 1500–1600 nm. The fiber is a promising design for mode division multiplexing (MDM) that supports the MIMO-free processing and improves the transmission capacity and spectral efficiency.**

***Index Terms*—Photonic crystal fiber, fiber communication system, polarization multiplexing, birefringence.**

I. Introduction

With the forthcoming capacity crunch of optical fiber communication system, mode division multiplexing (MDM) techniques have attracted great attention [1]. Based on mature multiplexing technologies such as time-division multiplexing (TDM), wavelength-division multiplexing (WDM) and space-division multiplexing (SDM) [2]–[4], MDM using different types of fiber modes provides another degree of freedom to increase the transmission capacity. Recently, most researchers focus on the study of linearly polarized modes (LP modes) [5], [6] and orbital angular momentum modes (OAM modes) [7]–[10]. The LP modes are composed of four-fold degenerate eigenmodes where $\mathrm{LP}_{n,1} = \mathrm{HE}_{n+1,1} + \mathrm{EH}_{n-1,1}$, and the OAM modes are composed of two-degenerate eigenmodes where $\mathrm{OAM}^{+}_{+n,1} = \mathrm{HE}^{odd}_{n+1,1} + i \times \mathrm{HE}^{even}_{n+1,1}$. Thus, mode coupling among the eigenmodes results in intermodal crosstalk during the transmission [11]. Therefore, multiple-input multiple-output digital signal processing (MIMO-DSP) technique is used to compensate for the induced crosstalk and dispersion that cause the system complexity and the power consumption. In addition, with the increase of the supported mode's number, the MIMO-DSP technique will be more complicated, leading to additional costs [12]–[14]. One way to eliminate the intermodal crosstalk and achieve a MIMO-free system is to separate the degenerate eigenmodes by enlarging the effective refractive index difference (Δn_{eff}) to the order of 10^{-4}, which keep the polarization-maintaining properties for short links [15], [16].

The key issue of MDM techniques is to select an appropriate orthogonal modal basis set for optical beams. The LP modes are amplitude orthogonal based on conventional weak waveguide fibers. The weak waveguide fiber supports the modes derived from the scalar wave equation, which ignores the refractive index gradient of fibers. Therefore, the LP modes have four-fold degenerate modes (HE^{odd}, HE^{even} or EH^{odd} , EH^{even}) which will induce crosstalk during transmission [17]. The OAM modes have orthogonal phase fronts, and the fiber supporting OAM modes have a ring-core with high refractive index contrast. The ring-shaped refractive index distribution breaks the weak waveguide condition and increases the Δn_{eff} between adjacent modes (HE, EH, TE, TM modes) [7]. However, each HE or EH mode still contains two degenerate even and odd eigenmodes, which will also bring mode coupling under external perturbations. Interestingly, the two even and odd eigenmodes are polarization orthogonal [17]. This leads to another type of orthogonal fiber eigenmodes used in MDM technology [18]. In addition to the ring-core with high refractive index contrast, by introducing the optical fiber's birefringence, the degenerate even and odd eigenmodes can be broken. So, one can design full vector polarization multiplexing fibers (FV-PMFs), which use full vector polarization modes (FV-PMs) as an alternative spatial mode basis set to achieve capacity scaling.

In principle, by adding stress-applying parts (SAPs) [19], using elliptical core [20], [21] or combining both ways together [16], [22]–[25], one can induce birefringence in designed fibers. In 2015, Wang and LaRochelle proposed an eight-mode polarization-maintaining few-mode fiber with an elliptical ring core [22]. This design supports higher-order modes only utilizing a small ellipticity (∼1.4). In 2017, researchers presented a PANDA ring-core fiber with 10 polarization-maintaining modes [24]. It has a ring-shaped fiber core with two SPAs. In the same

Manuscript received November 11, 2021; revised December 25, 2021; accepted January 5, 2022. Date of publication January 10, 2022; date of current version February 2, 2022. This work was supported in part by the National Key R&D Program of China under Grant 2020YFB1805800, in part by the National Natural Science Foundation of China under Grant 12034010, and in part by the National Key R&D Program of China under Grant 2017YFA0303800.
(Corresponding author: Yigang Li.)

The authors are with the School of Physics, Nankai University, Tianjin 300071, China (e-mail: nkweiwei@mail.nankai.edu.cn; 2120200243@mail.nankai.edu.cn; zhaohongyang@mail.nankai.edu.cn; 1120210097@mail.nankai.edu.cn; tanya@nankai.edu.cn; dinglei@nankai.edu.cn; liyigang@nankai.edu.cn).

This article has supplementary downloadable material available at https://doi.org/10.1109/JPHOT.2022.3141552, provided by the authors.

Digital Object Identifier 10.1109/JPHOT.2022.3141552

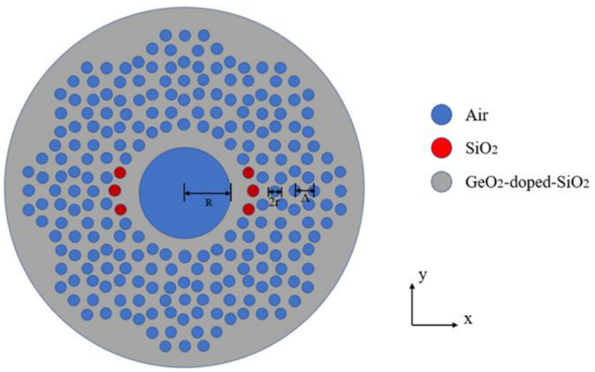

Fig. 1. Schematic cross section of the proposed RC-PQCF.

year, a polarization-maintaining supermode fiber with quasi-elliptically arranged high refractive index cores was proposed in [26]. This design supports 20 polarization modes and holds better manufacturing flexibility. In 2018, Wang *et al.* designed a PANDA-type elliptical-core multimode fiber supporting 24 fully lifted eigenmodes [19]. This design features an elliptical core inducing geometric birefringence and two symmetrical circular SAPs inducing stress birefringence. In [25], the same research group proposed a bow-tie elliptical ring-core multimode fiber. By combining the ring-core structure, elliptical core and bow-tie SAPs, this design can support 53 eigenmodes.

Compared with conventional fibers mentioned above, photonic crystal fiber has a unique arrangement of air holes. Due to the higher refractive index contrast and the good design flexibility, it is more convenient for PCFs to realize FV-PMs. In 2019, a photonic crystal fiber supporting fully separated eigenmodes was proposed [27]. This fiber can support 52 fully separated eigenmodes with $\Delta n_{eff} > 10^{-4}$ after optimization. However, the dispersion of eigenmodes is relatively large, which are not conducive to the transmission of fiber modes.

In this paper, we propose a ring-core photonic quasi-crystal fiber (RC-PQCF), which is characterized by a ring-shaped fiber core and two symmetrical SAPs. The fiber base is GeO_2-doped-SiO_2 and the SAPs is made of pure SiO_2. By adjusting the mole percentage of GeO_2 and optimizing the geometric parameters, the RC-PQCF supports 34 FV-PMs with minimum Δn_{eff} between adjacent modes larger than 1.07×10^{-4} at 1550 nm. We also discuss the dispersion (D_λ), effective mode area (A_{eff}) and nonlinearity (γ) of FV-PMs in the 1500–1600 nm, which indicate good broadband characteristics of RC-PQCF.

II. Fiber Structure

The schematic cross section and design parameters of RC-PQCF are shown in Fig. 1. The material of fiber is based on GeO_2-doped-SiO_2, as shown in the gray part of Fig. 1. The refractive index of this material is derived from hybrid Sellmeier equation, which dependents on the incident wavelength and the mole percentage (*m*) of GeO_2. The relationship can be expressed

TABLE I
Sellmeier Coefficients of SiO_2 From Malitson and GeO_2 From [28]

SA_1	Sl_1	SA_2	Sl_2	SA_3	Sl_3
0.69616630	0.0684043	0.40794260	0.11624140	0.8974794	9.896161
GA_1	Gl_1	GA_2	Gl_2	GA_3	Gl_3
0.80686642	0.068972606	0.71815848	0.15396605	0.85416831	11.841931

as follows:

$$n^2 - 1 = \sum_{i=1}^{i=3} \frac{[SA_i + m \times (GA_i - SA_i)]\lambda^2}{\lambda^2 - [Sl_i + m \times (Gl_i - Sl_i)]^2} \tag{1}$$

where *n* is the refractive index of GeO_2-doped-SiO_2, the value of i is from 1 to 3. SA_i and GA_i are the oscillator strength of SiO_2 and GeO_2 glasses, respectively; Sl_i and Gl_i are the oscillator wavelength of SiO_2 and GeO_2 glasses, respectively, the four parameters are fixed by their material, which is defined as sellmeier coefficients. *m* is the mole fraction of GeO_2, λ is the incident wavelength in the vacuum space. The corresponding coefficients are shown in Table I below. This type of model has been used in various binary glass system and has been well proven [28].

The fiber's cladding air holes are arranged in a structure of eight-fold photonic quasi-crystal, as the blue part shown in Fig. 1, where Λ is the air hole pitch (the distance between the centers of adjacent holes), r is the radius of the cladding air hole, and the duty cycle η is denoted as $2r/\Lambda$. By removing several rings of circular air holes in the center area and enlarging the radius of center air hole (*R*), it forms a ring-core fiber structure. In order to induce the birefringence effect, we replace the six air holes with SiO_2 rods symmetrically distributed on both sides of the center air hole. As the red part shown in Fig. 1. The addition of SiO_2 rods induces birefringence in the fiber, thereby lifting the separation degree of degenerate eigenmodes. The simulation is performed in a full-vector finite-element mode solver with a perfect matching layer (PML) as the boundary condition.

III. Fiber Parameters Optimization

In this section, we sweep the mole percentage of GeO_2 (*m*), the duty cycle η, the radius of center air hole (*R*), and the number of SiO_2 rods (*u*) to investigate the number and the min (Δn_{eff}) of FV-PMs at 1550 nm. Table II depicts the optimal design under different *m*. We change *m* from 5% to 40% with a step of 5%, when η, *R*, Λ and *u* remain 0.7, 9.4 μm, 4 μm and 6, respectively. From this table, we can see that when *m* = 30%, the number of FV-PM is the largest, which is 34 with the minimum $\Delta n_{eff} = 1.07 \times 10^{-4}$, and the doping concentration has been used for practical fabrication of high-birefringence fibers [25]. Table III lists the optimization of RC-PQCF under different η. When *m*, *R*, Λ and *u* remain 30%, 9.4 μm, 4 μm and 6, respectively, we set r from 1.15 μm to 1.48 μm, with a step of 0.05 μm and the corresponding η is from 0.575 to 0.74. The larger η results in a smaller gap between two adjacent air holes. In view of the limitations of fiber manufacturing technology, the gap should be larger than 100 nm, so we set maximum $r = 1.48$

TABLE II
OPTIMAL DESIGN SUPPORTING THE NUMBER OF FV-PMs WITH MINIMUM $\Delta n_{eff} > 10^{-4}$ UNDER DIFFERENT *m*

m	5%	10%	15%	20%
Mode number	16	18	20	28
Minimum Δn_{eff}	1.26e-4	1.16e-4	1.00e-4	1.23e-4
m	25%	30%	35%	40%
Mode number	30	34	32	31
Minimum Δn_{eff}	1.27e-4	1.07e-4	1.07e-4	1.00e-4

TABLE III
OPTIMAL DESIGN SUPPORTING THE NUMBER OF FV-PMs WITH MINIMUM $\Delta n_{eff} > 10^{-4}$ UNDER DIFFERENT η

η	0.575	0.6	0.625	0.65
Mode number	16	17	21	23
Minimum Δn_{eff}	1.04e-4	1.12e-4	1.02e-4	1.07e-4
η	0.675	0.7	0.725	0.74
Mode number	30	34	34	34
Minimum Δn_{eff}	1.10e-4	1.07e-4	1.26e-4	1.23e-4

TABLE IV
OPTIMAL DESIGN SUPPORTING THE NUMBER OF FV-PMs WITH MINIMUM $\Delta n_{eff} > 10^{-4}$ UNDER DIFFERENT *R*

R (μm)	9.1	9.2	9.3	9.4	9.5	9.6
Mode number	25	28	30	34	33	32
Minimum Δn_{eff}	1.10e-4	1.06e-4	1.09e-4	1.07e-4	1.18e-4	1.15e-4

μm, corresponding to $\eta = 0.74$. We can clearly see that when $\eta \leq 0.7$, the number of the FV-PMs increases with η to a maximum of 34. This is because the larger η increases the refractive index difference between the fiber core and the cladding region, and increases the separation between adjacent modes, thus the mode number of the RC-PQCF increases. By increasing η to 0.74, the number of FV-PMs remains 34, and there is no big change in Δn_{eff}. From above, η >0.7 will not lead to a better result while making the fabrication more difficult. Therefore, we set η to 0.7. Table IV displays optimal design under different *R*. We change *R* from 9.1 μm to 9.6 μm with a step of 0.1 μm, when *m*, η, Λ and *u* remain 30%, 0.7, 4 μm and 6, respectively. It can be seen that when R = 9.1∼9.4 μm, the mode number increases with the change of *R*; when R = 9.4∼9.6 μm, the mode number decreases with the change of *R*. Therefore, when $R = 9.4$ μm, the fiber supports the greatest number of FV-PMs with the minimum $\Delta n_{eff} = 1.07 \times 10^{-4}$. In the design, the number of SiO_2 rods (*u*) is an important parameter influencing

TABLE V
OPTIMAL DESIGN SUPPORTING THE NUMBER OF FV-PMs WITH MINIMUM $\Delta n_{eff} > 10^{-4}$ UNDER DIFFERENT *u*

Cross section	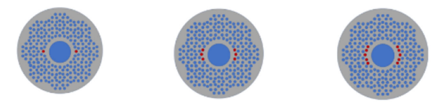		
u	2	6	10
Mode number	22	34	30
Minimum Δn_{eff}	1.02e-4	1.07e-4	1.08e-4

the transmission of FV-PMs. As we can see from Table V, when *m*, η, R and Λ remain 30%, 0.7, 9.4 μm, and 4 μm, respectively, we set u = 2, 6, and 10 (the corresponding schematic cross section is presented in the Table V), When $u = 2$, the supported FV-PMs is 22. It is because the *u* is not large enough to induce sufficient birefringence, and some degenerate FV-PMs can't be separated to the degree of 10^{-4}. When $u = 10$, the supported FV-PMs is 30, which is less than $u = 6$. It is because too many SiO_2 rods make the SAPs have higher circular symmetry, thereby reducing the degree of mode separation. So, 6 SiO_2 rods are the optimal design. In the end, we choose $m = 30\%$, $\eta = 0.7$, $R = 9.4$ μm, $u = 6$, and $\Lambda = 4$ μm to meet the requirement of minimum $\Delta n_{eff} > 10^{-4}$ and support as many FV-PMs as possible.

IV. MODE PROPERTIES AND BROADBAND CHARACTERISTICS

Using the optimized fiber design parameters, we show the transmission properties of 34 FV-PMs at 1500 nm. Fig. 2 represents the Intensity profiles with electric field polarization directions (black arrows) of 34 FV-PMs at 1550 nm. Compared with the traditional LP modes and OAM modes, we use $\mathbf{EM}_{\boldsymbol{n}}$ (n = 1∼34) to represent the FV-PMs, where *n* in the subscript refers to the mode order. When there is no SAPs, the ring-shaped fiber core separates the degenerate vector mode HE mode and EH mode, and supports the OAM modes. By setting two symmetric SiO_2-SAPs, the degenerate even and odd eigenmodes have a larger separation. When the $\boldsymbol{\Delta n_{eff}}$ between adjacent eigenmodes is larger than 10^{-4} , they form the EM modes. As shown in Fig. 2, the lower-order modes almost maintain the polarization directions of HE and EH modes, for the lower-order modes have smaller mode field diameter which suffer less effect of SAPs. The higher-order modes are almost linearly polarized. It is because the larger mode field diameters make them more susceptible to SAPs.

Table VI lists the Δn_{eff} (between EM_n and EM_{n+1}), dispersion (D_λ), confinement loss (α), mode field area (A_{eff}), and nonlinear coefficient (γ) of 34 FV-PMs at 1550 nm. The Δn_{eff} between all adjacent FV-PMs is larger than 1.07×10^{-4}. The D_λ of FV-PMs is within (44.24, 136.02) $\mathrm{ps \cdot nm^{-1} \cdot km^{-1}}$, where the EM_2 mode has the smallest dispersion of 44.24 $\mathrm{ps \cdot nm^{-1} \cdot km^{-1}}$ and the EM_{32} mode has the largest dispersion

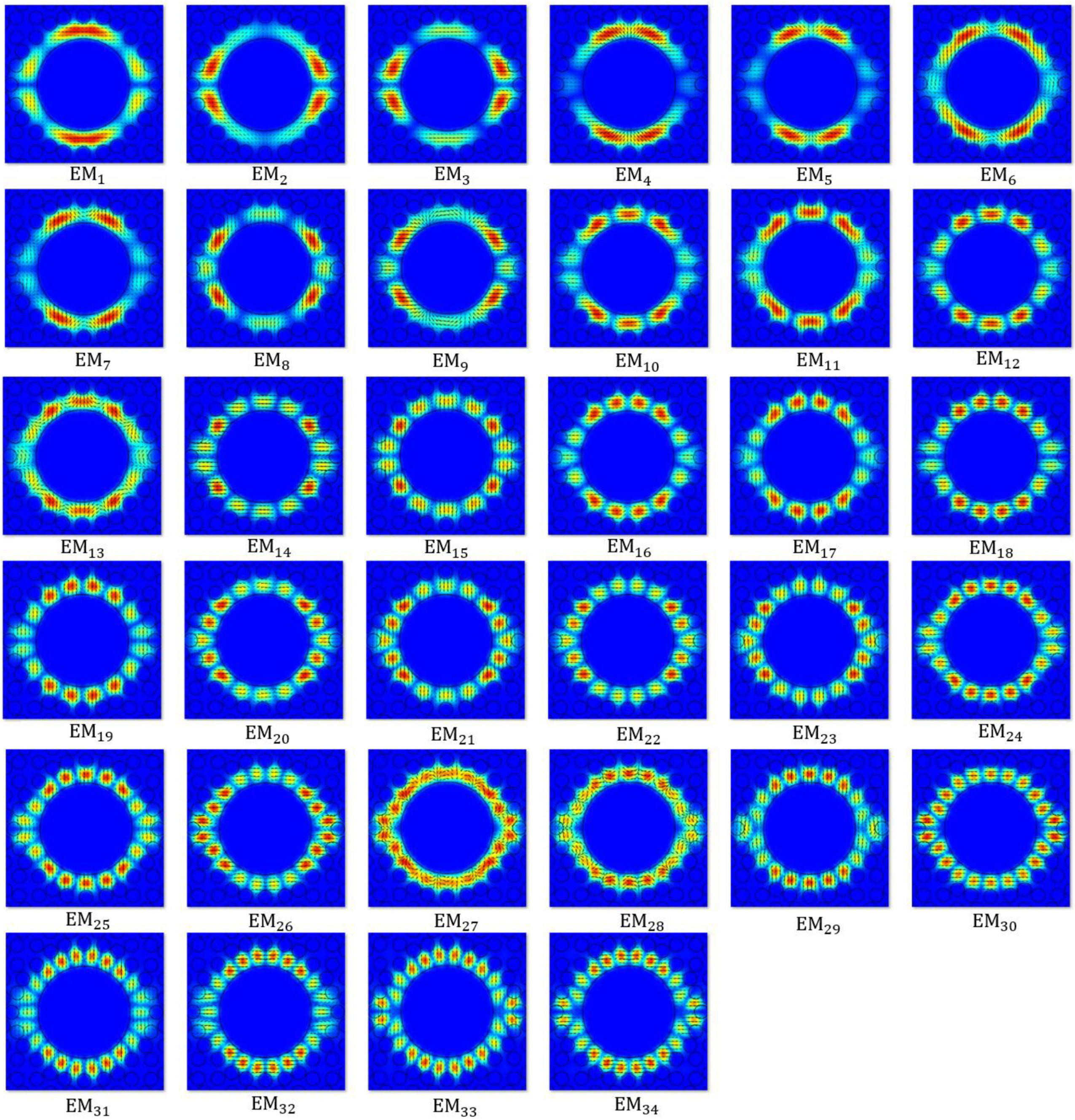

Fig. 2. Intensity profiles with electric field polarization directions (black arrows) of 34 FV-PMs at 1550 nm.

of 136.02 $\mathrm{ps \cdot nm^{-1} \cdot km^{-1}}$. It is conducive to the stable transmission of FV-PMs. For α, the EM_8 mode has the minimum α of 2.16×10^{-12} $\mathrm{dB \cdot km^{-1}}$, and the EM_{34} mode has the maximum α of 1.11×10^{-6} $\mathrm{dB \cdot km^{-1}}$. The order of FV-PMs' α is less than 10^{-6}, which is sufficient to limit the light field in the ring-core and suppresses the high leakage loss. The A_{eff} of FV-PMs is within (90.74, 187.55) $\mu\mathrm{m}^2$, in which the EM_5 mode has the smallest A_{eff} of 90.74 $\mu\mathrm{m}^2$ and the EM_{27} mode has the largest A_{eff} of 187.55 $\mu\mathrm{m}^2$. Compared with other proposed polarization maintaining fibers, the RC-PQCF has a relatively larger A_{eff}. The γ of FV-PMs is within (6.81×10^{-4}, 1.41×10^{-3}) $\mathrm{m^{-1} \cdot W^{-1}}$ which is low enough to suppress nonlinear effects in RC-PQCF.

We further investigate the wavelength dependence of 34 FV-PMs in the 1500–1600 nm. In Fig. 3(a), the left figure is the effective refractive index (n_{eff}) of EM_1 to EM_{17}, and the right figure is the n_{eff} of EM_{18} to EM_{34}. It can be clearly seen from Fig. 3(a) that the n_{eff} of FV-PMs decreases with the increase of wavelength. Higher-order FV-PMs have lower n_{eff} at the same wavelength. It coincides with the conventional ring-shaped

TABLE VI
Δn_{eff}, D_λ, α, A_{eff}, AND γ OF 34 FV-PMs AT 1550 nm

Mode	Δn_{eff}	D_λ (ps · nm^{-1} · km^{-1})	α (dB · km^{-1})	A_{eff} (μm^2)	γ (m^{-1} · W^{-1})
EM_1	1.61e-4	45.97	9.97e-9	128.58	9.93e-4
EM_2	1.98e-4	44.24	9.08e-10	111.98	1.14e-3
EM_3	1.15e-4	45.71	1.30e-8	109.23	1.17e-3
EM_4	1.55e-4	57.39	2.51e-11	102.29	1.25e-3
EM_5	1.07e-4	57.22	3.47e-11	90.74	1.41e-3
EM_6	3.34e-4	54.78	1.03e-10	135.31	9.43e-4
EM_7	5.25e-4	56.60	5.38e-11	102.53	1.24e-3
EM_8	1.74e-4	57.41	2.16e-12	107.08	1.19e-3
EM_9	1.17e-3	60.44	1.48e-10	124.29	1.03e-3
EM_{10}	3.35e-4	62.77	2.23e-10	116.37	1.10e-3
EM_{11}	7.07e-4	65.28	1.33e-9	130.29	9.80e-4
EM_{12}	2.91e-4	68.72	2.08e-11	115.17	1.11e-3
EM_{13}	1.53e-3	68.36	5.12e-11	152.05	8.39e-4
EM_{14}	1.36e-4	76.26	2.31e-10	122.00	1.05e-3
EM_{15}	5.56e-4	77.77	2.93e-10	131.08	9.74e-4
EM_{16}	2.08e-4	78.82	5.03e-12	114.65	1.11e-3
EM_{17}	1.09e-3	80.29	7.40e-12	112.59	1.13e-3
EM_{18}	1.43e-4	87.08	1.41e-10	121.08	1.05e-3
EM_{19}	1.36e-3	87.40	5.13e-10	116.94	1.09e-3
EM_{20}	2.08e-4	85.76	9.30e-10	121.55	1.05e-3
EM_{21}	1.17e-3	87.97	7.85e-11	121.59	1.05e-3
EM_{22}	1.20e-4	92.37	1.59e-9	124.42	1.03e-3
EM_{23}	1.10e-3	93.26	2.78e-10	127.88	9.98e-4
EM_{24}	2.92e-4	101.46	1.30e-10	128.17	9.96e-4
EM_{25}	1.76e-3	102.90	1.09e-11	125.94	1.02e-3
EM_{26}	1.29e-4	106.62	4.97e-10	129.06	9.89e-4
EM_{27}	1.54e-4	105.44	3.75e-10	187.55	6.81e-4
EM_{28}	1.69e-4	106.81	8.66e-10	171.42	7.45e-4
EM_{29}	2.15e-3	73.87	4.36e-10	125.38	1.02e-3
EM_{30}	1.36e-3	118.20	5.22e-11	133.00	9.60e-4
EM_{31}	1.88e-4	129.82	1.95e-9	114.32	1.12e-3
EM_{32}	9.38e-4	136.02	1.04e-8	117.64	1.08e-3
EM_{33}	1.86e-4	118.04	7.36e-8	130.02	9.82e-4
EM_{34}	----	129.33	1.11e-6	128.27	9.95e-4

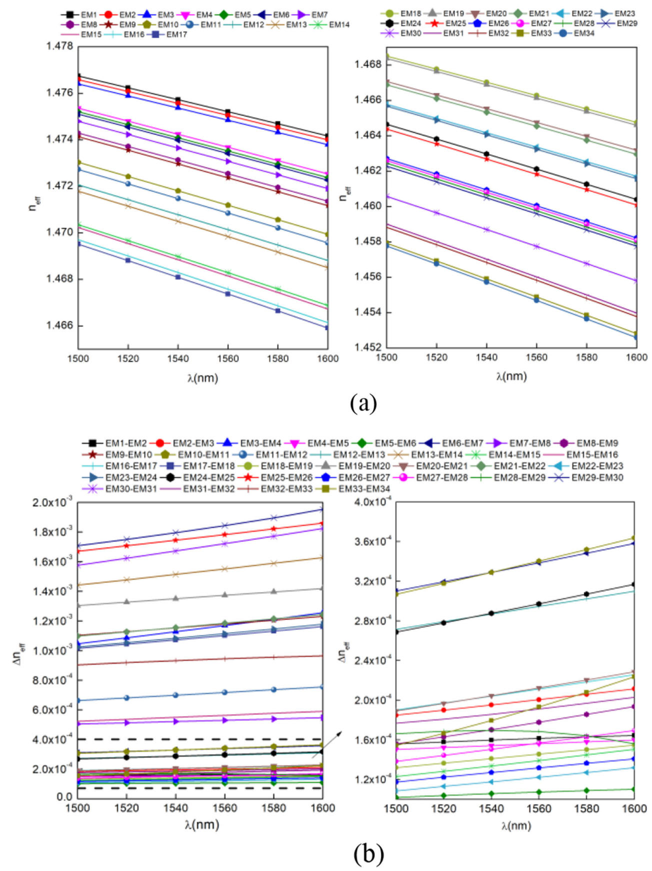

Fig. 3. (a) n_{eff} of FV-PMs as a function of wavelength; (b) Δn_{eff} of adjacent FV-PMs as a function of wavelength.

optical fiber. Fig. 3(b) shows the Δn_{eff} of adjacent FV-PMs as a function of wavelength. The figure on the right is an enlarged view of the black dashed box in the left figure. The Δn_{eff} of adjacent FV-PMs increases with the increase of wavelength except for the Δn_{eff} between EM_{28} and EM_{29}. The minimum Δn_{eff} of 34 FV-PMs is 1.07×10^{-4} that lies between EM_5 and EM_6 mode at 1500 nm. Within the 1500–1600 nm, the Δn_{eff} of all FV-PMs is above 10^{-4} which has good broadband characteristics.

The D_λ of FV-PMs in the 1500–1600 nm is shown in Fig. 4(a), the D_λ of FV-PMs gradually increases with the wavelength except for the EM_{29}, EM_{30}, and EM_{33} modes. As the increase of mode order, the D_λ is relatively higher. The highest dispersion is 138.14 $\mathrm{ps} \cdot \mathrm{nm}^{-1} \cdot \mathrm{km}^{-1}$ belongs to the EM_{32} mode at 1600 nm, and the lowest dispersion is 35.88 $\mathrm{ps} \cdot \mathrm{nm}^{-1} \cdot \mathrm{km}^{-1}$ belongs to the EM_{29} mode at 1600 nm. Except for the EM_{29} mode, the rest of FV-PMs maintain a flat trend, and the dispersion variation of the single FV-PM is less than 11.38 $\mathrm{ps} \cdot \mathrm{nm}^{-1} \cdot \mathrm{km}^{-1}$. The dispersion properties are conducive to the short-reach optical interconnection. Fig. 4(b) presents the A_{eff} of FV-PMs in the 1500–1600 nm. Except for the EM_1, EM_2, EM_{27}, EM_{31}, EM_{32} modes, the A_{eff} of other FV-PMs increases slightly with the wavelength. The largest A_{eff} falls at 1500 nm of the EM_{27} mode, which is 188.19 μm^2, and the smallest A_{eff} falls at 1500 nm of the EM_5 mode, which is 90.38 μm^2. In short, the A_{eff} is relatively larger than single-mode fibers and other proposed polarization-maintaining fibers. Fig. 4(c) represents the γ of FV-PMs in the 1500–1600 nm. Except for the EM_1 mode, the γ of FV-PMs decreases with the increase of wavelength. The EM_5 mode has the largest γ of 1.54×10^{-3} $\mathrm{m}^{-1} \cdot \mathrm{W}^{-1}$ at 1500 nm,

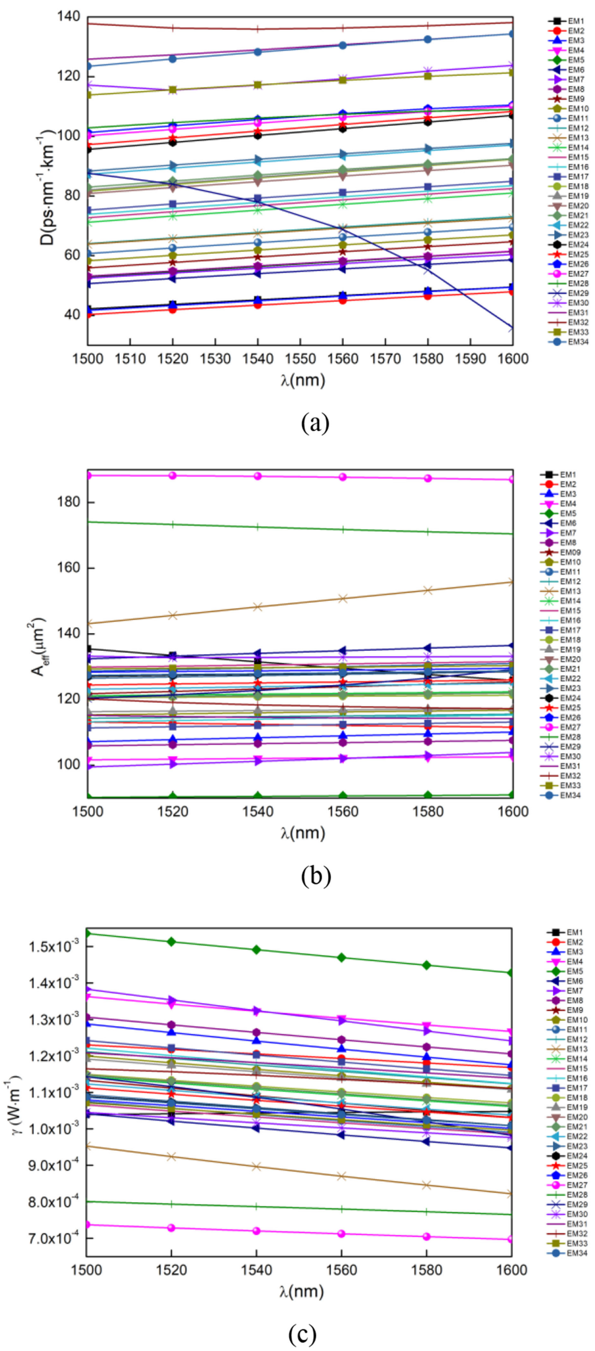

Fig. 4. (a) D_λ, (b) A_{eff}, (c) γ of FV-PMs as a function of wavelength.

and the EM_{27} mode has the lowest γ of $6.97 \times 10^{-4}\,\mathrm{m}^{-1} \cdot \mathrm{W}^{-1}$ at 1600 nm.

V. Conclusion

In conclusion, we propose a RC-PQCF with 34 FV-PMs for MDM. The fiber base is GeO_2-doped-SiO_2 with 30% mole percentage, and the fiber has a ring-shaped fiber core with SAPs made of pure SiO_2. We use the full-vector finite-element method to analyze the transmission characteristics of FV-PMs. By optimizing, the adjacent FV-PMs eventually achieve a large effective refractive difference ($\Delta n_{eff} > 10^{-4}$). For the broadband characteristics (1500–1600 nm), the dispersion of FV-PMs is lower than $138.14\,\mathrm{ps} \cdot \mathrm{nm}^{-1} \cdot \mathrm{km}^{-1}$ and maintains a flat trend, except for the EM_{29} mode. the α of FV-PMs is less than $1.11 \times 10^{-6}\,\mathrm{dB} \cdot \mathrm{km}^{-1}$. The A_{eff} of FV-PMs is within (90.38, 188.19) $\mu\mathrm{m}^2$ and the γ of FV-PMs is within (6.97×10^{-4}, 1.54×10^{-3}) $\mathrm{m}^{-1} \cdot \mathrm{W}^{-1}$. This design will be compatible with current multiplexing techniques. It can be employed in low-crosstalk polarization multiplexing system with MIMO-free processing.

The practical fiber manufacture technologies have been well-developed. The structure of RC-PQCF can be made with a die-cast method proposed in [29]. By tailoring a heat-resisting alloy steel die of the RC-PQCF preform, the PCF will be drawn. The SAPs have been widely used on PANDA type fibers to maintain mode polarizations. So, the manufacture technologies are relatively mature, which provide a solid foundation for the manufacture of RC-PQCF. In addition, our design only uses the ring-shaped fiber core structure and the SAPs components. In future designs, we can induce larger geometric birefringence in fibers, just like an elliptical ring-shaped fiber core to increase Δn_{eff} and further suppress the crosstalk. Meanwhile, the photonic crystal fiber has more design flexibility. By optimizing the geometrical parameters, the corresponding broadband characteristics we need will be achieved.

References

[1] D. J. Richardson, J. M. Fini, and L. E. Nelson, "Space-division multiplexing in optical fibres," *Nature Photon.*, vol. 7, no. 5, pp. 354–362, May 2013, doi: 10.1038/nphoton.2013.94.

[2] S. Yan *et al.*, "Archon: A function programmable optical interconnect architecture for transparent intra and inter data center SDM/TDM/WDM networking," *J. Lightw. Technol.*, vol. 33, no. 8, pp. 1586–1595, Apr. 2015, doi: 10.1109/JLT.2015.2392554.

[3] S. Yu, "Potentials and challenges of using orbital angular momentum communications in optical interconnects," *Opt. Exp.*, vol. 23, no. 3, pp. 3075–3067, Feb. 2015, doi: 10.1364/OE.23.003075.

[4] E. Ip *et al.*, "SDM transmission of real-time 10GbE traffic using commercial SFP + transceivers over 0.5km elliptical-core few-mode fiber," *Opt. Exp.*, vol. 23, no. 13, pp. 17120–17126, Jun. 2015, doi: 10.1364/OE.23.017120.

[5] S. Randel *et al.*, "6×56-Gb/s mode-division multiplexed transmission over 33-km few-mode fiber enabled by 6×6 MIMO equalization," *Opt. Exp.*, vol. 19, no. 17, pp. 16697–16707, Aug. 2011, doi: 10.1364/OE.19.016697.

[6] R. Ryf *et al.*, "Mode-multiplexed transmission over conventional graded-index multimode fibers," *Opt. Exp.*, vol. 23, no. 1, pp. 235–246, Jan. 2015, doi: 10.1364/OE.23.000235.

[7] A. E. Willner *et al.*, "Optical communications using orbital angular momentum beams," *Adv. Opt. Photon.*, vol. 7, no. 1, pp. 66–106, Mar. 2015, doi: 10.1364/AOP.7.000066.

[8] H. Zhang, W. Zhang, L. Xi, X. Tang, X. Zhang, and X. Zhang, "A new type circular photonic crystal fiber for orbital angular momentum mode transmission," *IEEE Photon. Technol. Lett.*, vol. 28, no. 13, pp. 1426–1429, Jul. 2016, doi: 10.1109/LPT.2016.2551325.

[9] Z.-A. Hu, Y.-Q. Huang, A.-P. Luo, H. Cui, Z.-C. Luo, and W.-C. Xu, "Photonic crystal fiber for supporting 26 orbital angular momentum modes," *Opt. Exp.*, vol. 24, no. 15, pp. 17285–17291, Jul. 2016, doi: 10.1364/OE.24.017285.

[10] W. Wei, N. An, Z. Zhang, L. Tang, L. Ding, and Y. Li, "Design of a microstructure optical fiber supporting 52 vortex beams," *Opt. Commun.*, vol. 490, Jul. 2021, Art. no. 126657, doi: 10.1016/j.optcom.2020.126657.

[11] Y. Yue *et al.*, "Mode properties and propagation effects of optical orbital angular momentum (OAM) modes in a ring fiber," *IEEE Photon. J.*, vol. 4, no. 2, pp. 535–543, Apr. 2012, doi: 10.1109/JPHOT.2012.2192474.

[12] S. O. Arik, D. Askarov, and J. M. Kahn, "Adaptive frequency-domain equalization in mode-division multiplexing systems," *J. Lightw. Technol.*, vol. 32, no. 10, pp. 1841–1852, May 2014, doi: 10.1109/JLT.2014.2303079.

[13] P. Sillard, D. Molin, M. Bigot-Astruc, A. Amezcua-Correa, K. de Jongh, and F. Achten, "50 μm multimode fibers for mode division multiplexing," *J. Lightw. Technol.*, vol. 34, no. 8, pp. 1672–1677, Apr. 2016. [Online]. Available: https://www.osapublishing.org/jlt/abstract.cfm?uri=jlt-34-8-1672

[14] T. Hayashi *et al.*, "Six-mode 19-core fiber with 114 spatial modes for weakly-coupled mode-division-multiplexed transmission," *J. Lightw. Technol.*, vol. 35, no. 4, pp. 748–754, Feb. 2017. [Online]. Available: https://www.osapublishing.org/jlt/abstract.cfm?uri=jlt-35-4-748

[15] J. Noda, K. Okamoto, and Y. Sasaki, "Polarization-maintaining fibers and their applications," *J. Lightw. Technol.*, vol. 4, no. 8, pp. 1071–1089, Aug. 1986, doi: 10.1109/JLT.1986.1074847.

[16] L. Wang *et al.*, "Linearly polarized vector modes: Enabling MIMO-free mode-division multiplexing," *Opt. Exp.*, vol. 25, no. 10, May 2017, Art. no. 11736, doi: 10.1364/OE.25.011736.

[17] S. Ramachandran and P. Kristensen, "Optical vortices in fiber," *Nanophotonics*, vol. 2, no. 5–6, pp. 455–474, Dec. 2013, doi: 10.1515/nanoph-2013-0047.

[18] A. E. Willner, "Vector-mode multiplexing brings an additional approach for capacity growth in optical fibers," *Light Sci. Appl.*, vol. 7, no. 3, pp. 18002–18002, Mar. 2018, doi: 10.1038/lsa.2018.2.

[19] S. Chen and J. Wang, "Design of PANDA-type elliptical-core multimode fiber supporting 24 fully lifted eigenmodes," *Opt. Lett.*, vol. 43, no. 15, pp. 3718–3721, Aug. 2018, doi: 10.1364/OL.43.003718.

[20] L. Junpeng, Q. Mo, S. Fu, M. Tang, P. Shum, and D. Liu, "Design and fabrication of elliptical-core few-model-41-13-3058," *Opt. Lett.*, vol. 41, 2016, Art. no. 3058.

[21] L. Wang *et al.*, "MDM transmission of CAP-16 signals over 11-km anti-bending trench-assisted elliptical-core few-mode fiber in passive optical networks," *Opt. Exp.*, vol. 25, no. 19, Sep. 2017, Art. no. 22991, doi: 10.1364/OE.25.022991.

[22] L. Wang and S. LaRochelle, "Design of eight-mode polarization-maintaining few-mode fiber for multiple-input multiple-output-free spatial division multiplexing," *Opt. Lett.*, vol. 40, no. 24, pp. 5846–5849, Dec. 2015, doi: 10.1364/OL.40.005846.

[23] L. Wang *et al.*, "MIMO-free transmission over six vector modes in a polarization maintaining elliptical ring core fiber," in *Proc. 2017 Optical Fiber Commun. Conf. Exhib. (OFC)*, 2021. [Online]. Available: https://ieeexplore.ieee.org/abstract/document/7937210

[24] H. Yan, S. Li, Z. Xie, X. Zheng, H. Zhang, and B. Zhou, "Design of PANDA ring-core fiber with 10 polarization-maintaining modes," *Photon. Res.*, vol. 5, no. 1, pp. 1–5, Feb. 2017, doi: 10.1364/PRJ.5.000001.

[25] S. Chen and J. Wang, "Fully degeneracy-lifted bow-tie elliptical ring-core multi-mode fiber," *Opt. Exp.*, vol. 26, no. 14, pp. 18773–18782, Jul. 2018, doi: 10.1364/OE.26.018773.

[26] H. Xiao *et al.*, "Polarization-maintaining supermode fiber supporting 20 modes," *IEEE Photon. Technol. Lett.*, vol. 29, no. 16, pp. 1340–1343, Aug. 2017, doi: 10.1109/LPT.2017.2722226.

[27] S. Chen and J. Wang, "Photonic crystal fibers supporting fully separated eigenmodes," *Opt. Lett.*, vol. 44, no. 12, pp. 3046–3049, Jun. 2019, doi: 10.1364/OL.44.003046.

[28] J. W. Fleming, "Dispersion in GeO_2–SiO_2 glasses," *Appl. Opt.*, vol. 23, no. 24, pp. 4486–4493, Dec. 1984, doi: 10.1364/AO.23.004486.

[29] Z. Guiyao, H. Zhiyun, L. Shuguang, and H. Lantian, "Fabrication of glass photonic crystal fibers with a die-cast process," *Appl. Opt.*, vol. 45, no. 18, pp. 4433–4436, Jun. 2006, doi: 10.1364/AO.45.004433.